Transition to efficient, unsuppressed bulk-target ion acceleration via high-fluence laser irradiation

D. P. Higginson,[1,2] J. Kim,[2] G. M. Petrov,[3] D. C. Swift,[1] J. A. Cobble,[4] D. L. Bleuel,[1] J. A. Frenje,[5] V. Yu. Glebov,[6] C. Stoeckl,[6] J. M. McNaney,[1] and F. N. Beg[2]

[1]*Lawrence Livermore National Laboratory, Livermore, California 94551, USA*
[2]*Center for Energy Research, University of California, San Diego, California 92093, USA*
[3]*Naval Research Laboratory, Plasma Physics Division, Washington DC 20375, USA*
[4]*E-526, Los Alamos National Laboratory, Los Alamos, New Mexico 87545, USA*
[5]*Plasma Science and Fusion Center, Massachusetts Institute of Technology, Cambridge, Massachusetts 02139, USA*
[6]*Laboratory for Laser Energetics, University of Rochester, Rochester, New York 14623, USA*

(Received 23 October 2021; accepted 27 June 2022; published 10 August 2022)

A high-intensity laser irradiating a few-μm solid foil will accelerate ions from the bulk of the target as well as protons from a surface contaminant layer. Experimental measurements of ion spectra using the OMEGA EP laser (0.25–1 kJ, 10 ps) show, as suggested previously [Petrov *et al.*, Phys. Plasmas **17**, 103111 (2010)], that at a laser fluence exceeding 1 J/μm^2, the contaminant layer is accelerated enough that ions from the bulk of the target are more effectively accelerated. When using CD_2 as a target, the high fluence results in a 100-fold increase in deuteron acceleration efficiency (near 1% of laser energy) compared to subthreshold fluence. This is found to be due to the fact that the deuterons have a higher density at many locations during acceleration, allowing a larger electric field to develop, leading to improved efficiency. Using a pitcher-catcher setup, these deuterons, as well as protons from the contaminant layer, strike a LiF target and generate neutrons via (*d,n*) and (*p,n*) nuclear reactions. CR39 plastic and nuclear activation detectors measured broadband neutron yields of 4×10^9 sr^{-1} and yields of 10^8 sr^{-1} for neutrons above 11 MeV.

DOI: 10.1103/PhysRevResearch.4.033113

I. INTRODUCTION

The acceleration of multi-MeV ions via short-pulse, high-intensity laser irradiation of solid targets has been well-studied [1–5] over the last few decades. These ions have proven to be extremely useful, for instance, to diagnose electromagnetic fields [6–9], to deposit energy for ion fast ignition research [10–12], to isochorically heat solid material [13], and to generate ultrashort bursts of high-energy neutrons [14–19]. Such neutrons can be used to understand atomic-scale damage [20] and are important for applications related to semiconductor radiation hardness testing, materials for fusion or fission reactors, particle accelerator vessels, and long-term radioactive nuclear waste storage [21–23]. These neutrons also have the potential to diagnose ion temperature and flow velocity in materials under extreme conditions via neutron resonance spectroscopy [15,24] with short temporal resolution.

The most widely used mechanism for ion acceleration is known as target normal sheath acceleration (TNSA) [25]. In TNSA, multi-MeV electrons accelerated by a relativistic-intensity ($I\lambda_L^2 > 10^{18}$ W cm$^{-2}\mu$m^2) laser [26] form an electrostatic sheath on the rear of the target that accelerates ions normal to the rear side of the target surface. While ions from the bulk of the target are accelerated, both the efficiency and peak energy of these ions are substantially reduced owing to a thin, few-nm hydrocarbon contaminant layer on the target surface [27,28]. Protons in the contaminant layer impede bulk-ion acceleration due to their high charge-to-mass ratio and their location on the outermost surface, which shields the bulk target from the highest electric fields. For this reason, a variety of techniques have been employed to remove contaminants (e.g., resistive-heating [29], ion-sputtering [27], and laser-heating [11]), including techniques developed specifically to preferentially accelerate deuterons [30,31] for use in neutron generation [32,33]. Alongside these advances, other ion acceleration techniques, such as front-surface ion acceleration [34–36], and advanced ion acceleration mechanisms such as break-out afterburner (BOA) [37,38] have been studied to generate neutrons [17,39]. While these techniques are effective, they introduce additional experimental components or require state-of-the-art laser conditions (e.g., extremely high contrast for BOA). Such methods are feasible at small- to medium-scale facilities, but it is not simple to implement these on the largest scale facilities, such as the 14 kJ ARC [40–42] laser at the National Ignition Facility and the 6 kJ PETAL [43,44] laser at Laser MegaJoule. Despite the somewhat lower laser intensity compared to the BOA regime, recent work [45–47] has shown that these lasers can accelerate ions efficiently due to the longer pulse duration. Additionally, it is at these facilities that ion acceleration can make the largest impact as higher ion energy and flux can be attained. These lasers can be used as diagnostics of the extreme high-energy-density conditions created by co-located nanosecond lasers

as intense sources of isochoric energy deposition to create astrophysically relevant warm-density-matter conditions [48] and, as we specifically discuss in this paper, as a mechanism to generate short, bright pulses of neutrons. By optimizing the laser parameters to deplete the contaminant layer itself, without additional components, it will be possible to generate the cleanest, most contaminant-free, ion acceleration on these large-scale facilities.

Much TNSA research has focused on increasing the laser intensity, often by using shorter laser pulses, to reach higher peak ion energies. This focus on high *intensity* has meant that the regime of few-picosecond duration lasers with high *fluence* has, largely, been neglected [49]. The advantage of higher fluence is that the total energy coupled is increased [5], which can lead to regimes of acceleration that deplete the approximately 1-nm-thick [27,28] contaminant layer and thus allow bulk ions from the target to be accelerated. Previous work, simulating a CD bulk target with an H_2O contaminant layer by Petrov *et al.* [50], showed that at a laser fluence of 0.1 J/μm^2 the contaminant layer began to be depleted and at 1 J/μm^2 the bulk target deuterons dominated the ion acceleration.

The physics of TNSA is known to be described by a self-similar adiabatic expansion [51–53]; that is, the expansion of the plasma and subsequent ion acceleration is driven by an electron-pressure driven electric field. This self-similar electric field, $E_{ss} \propto T_e/C_{si} = (T_e m_i/Z_i)^{1/2}$, is a function of the electron temperature, T_e, and the ion acoustic velocity $C_{si} = (Z_i T_e/m_i)^{1/2}$, which is in turn a function of ion charge, Z_i, and mass, m_i. There are important deviations in the electric field due to charge separation at the leading edge of the plasma acceleration, but these fields are still proportional to the self-similar field [53]. This means that, alone, a heavier (larger m_i/Z_i) species will create a stronger electric field than a lighter species. However, when there are two ion species, the ions with the highest density set the electric field [54,55]. Thus, in the case of a contaminant layer of protons with a CD_2 target, the electric field is reduced compared to what would be expected if deuterons were the only species.

In this paper, we present experimental evidence of what has been described as contaminant layer depletion using a high-fluence, kilojoule class laser. This is confirmed by measuring the ion spectrum from a CD target irradiated by a laser of fluence exceeding the critical level of 1 J/μm^2. We observe a substantial increase in the deuteron acceleration efficiency up to $0.6 \pm 0.1\%$ and see a dip in low energies in the proton spectrum that corresponds to half the peak energy of the deuterons. However, unlike previous work, we do not describe this as depletion of the contaminant layer, which implies that all the contaminants are removed from the target's rear surface. Instead, our simulations show that the protons are still present at the rear surface of the target, but they are at a lower density than the deuterons. This deuteron-rich region causes a transition from suppressed to unsuppressed deuteron acceleration, meaning that high laser fluence causes increased proton expansion leading to a region of lowered proton density. In this region, the electric field increases, leading to a higher deuteron slope temperature and acceleration efficiency.

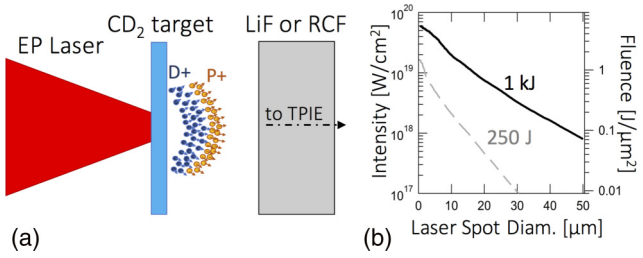

FIG. 1. (a) Experimental schematic. Ions (protons, deuterons) are accelerated from a 25-μm-thick CD_2 target by the OMEGA EP laser. To study the ions, RCF and the TPIE are used as diagnostics. For neutron generation, a LiF converter is placed in the path of the ions to generate neutrons via (*p,n*) and (*d,n*) reactions. (b) Spatial laser intensity (left axis) and fluence (right axis) profiles at laser energies of 250 J (dashed line) and 1 kJ (solid line); note that 50% and 90% of the laser energy is contained within diameters of 20 and 60 μm, respectively. Only in the 1 kJ case is a significant fraction of the laser fluence above the 1 J/μm^2 contaminant depletion threshold [50].

II. EXPERIMENTAL SETUP

In the experiment, the deuterons, and protons from the contaminant layer, subsequently interact with a secondary LiF target to produce neutrons via (*d,n*) and (*p,n*) reactions with a fluence up to 4×10^9 neutrons per steradian. To understand the impact of the enhanced deuteron acceleration on neutron generation, the CD_2 target was replaced with Cu for some shots. Neutron yields were found to be higher in the CD_2 + LiF case relative to the Cu + LiF case. This was especially true for the highest energy (>11 MeV) neutrons, as the ^{7}Li(*d,n*) reaction is exothermic, while ^{7}Li(*p,n*) is endothermic.

The experiment was performed on the 1 μm wavelength, 9 ps duration, OMEGA EP laser at the Laboratory for Laser Energetics in Rochester, NY, at laser energies (peak intensities) of 250 J (1.5×10^{19} W/cm^2) and 1.0 kJ (6×10^{19} W/cm^2). The laser intensity and fluence profiles are shown in Fig 1(a), where we note that 50% and 90% of the laser energy is contained within diameters of 20 and 60 μm, respectively. About half the laser energy in the 1 kJ case is within a spot that exceeds the fluence of 1 J/μm^2, which has been shown to be the threshold for high-efficiency bulk-target acceleration [50]. On the other hand, in the 250 J case, the portion of the laser spot above a fluence of 1 J/μm^2 is negligible. Characterization of the laser prepulse is found in Ref. [56]. The experimental setup for neutron generation is shown in Fig 1(b), where the laser irradiates a 25 μm CD_2 target that is positioned next to a 2 mm LiF slab in which neutrons are produced via (*d,n*) and (*p,n*) reactions. This LiF slab was removed for measurement of the ion spectrum. Also, for some shots the CD_2 target was replaced with Cu to observe neutron generation from protons alone.

III. EXPERIMENTAL RESULTS

A Thomson parabola ion energy analyzer (TPIE) [57] was used to measure the spectra and quantity of the ion species accelerated from the rear surface of the target. The measured

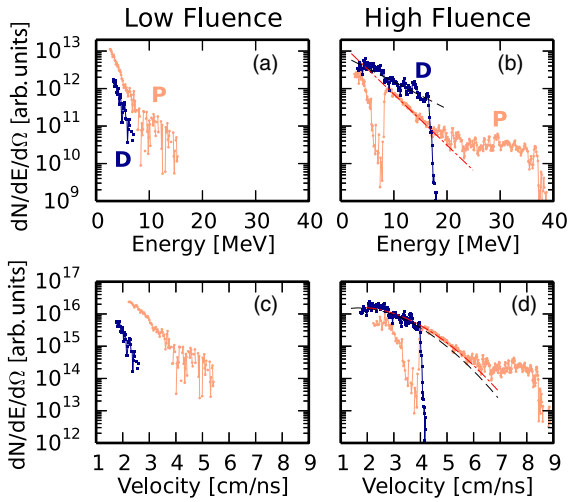

FIG. 2. TPIE measurements of the ion energy (a), (b) and velocity (c), (d) spectra in the low-fluence [250 J; (a), (c)] and high-fluence [1 kJ; (b), (d)] cases. The units are directly proportional to the ion fluence. Protons (P) are plotted as circles and deuterons (D) as squares. The lines in (b), (d) represent exponential decays in energy [$\frac{dN}{dEd\Omega} \propto \exp(-E/T)$] with characteristic temperatures, T, of 5.6 (dashed line) and 3.3 MeV (dash-dotted line) for the deuterons and protons, respectively.

ion energy spectra for the 250 J and 1 kJ cases are shown in Figs. 2(a) and 2(b), respectively. The signals are corrected for the ion-dependent energy response of the diagnostic; thus the units are directly proportional to the number of ions in a manner similar to Ref. [58]. In the low fluence case (250 J), a monotonically decaying exponential spectra is observed for both ions species as expected from TNSA. In the 1 kJ case, the spectra change significantly; the proton spectrum develops a dip at energy around 8 MeV. Additionally, the relative number of deuterons compared to protons is increased by an order of magnitude as compared with the 250 J case. As shown in Table I, increasing the laser energy increases the maximum energy of both protons (from 15 MeV to 38 MeV) and deuterons (from 5 MeV to 18 MeV). The ratio of deuteron to proton maximum energy increases from 1:3 (33%) to 1:2.1 (47%); again suggesting increased bulk-target ion acceleration. To better understand these features, the energy spectrum was transformed to a velocity spectrum and shown in Figs. 2(c) and 2(d). A particularly interesting observation from the high fluence data [Fig. 2(d)] is that, in velocity space, the transition between deuteron and proton spectra is remarkably continuous; meaning that at around 4 cm/ns the deuterons spectra sharply ends and the proton spectra sharply rises. As we will show later in the simulations, this sharp change is a characteristic of the transition between deuteron-rich and proton-rich spatial regions where the acceleration is occurring.

TABLE I. Metrics of proton and deuteron acceleration from the OMEGA EP experiment. The laser energy, E_{laser}, ion acceleration efficiency, η, in the forward direction, exponential fit to the ion temperature, T, and maximum ion energy, $E^{\max}$.

E_{laser} J	η_P %	η_D %	T_P MeV	T_D MeV	$E_P^{\max}$ MeV	$E_D^{\max}$ MeV
250	1.0	0.006	1.31	1.09	15	5
1000	4.5	0.6	3.33	5.49	38	18

Fitting the energy, E, spectra with exponential decays ($\propto \exp[-E/T]$) results in a characteristic temperature, T, of 5.6 MeV for the deuterons, which is almost exactly twice that of the protons. Thus, once the energy spectra are converted into velocity spectra, the effective slopes of the two ion species are nearly identical. Using radiochromic film (RCF) [59], laser-to-proton conversion efficiencies of 1% and 4.5% were measured for the 250 J and 1 kJ cases, respectively, considering protons above 4.8 MeV, the RCF minimum energy. The laser-to-deuteron efficiency was inferred from measurements of high-energy neutrons (>11 MeV) produced by (d,n) reactions in the LiF converter (to be explained in detail later); it was found to be $0.6 \pm 0.1\%$ in the 1 kJ case. Assuming a constant ratio of divergence angle between protons and deuterons gave $6 \times 10^{-3}\%$ in the 250 J case; meaning a 100× increase in conversion of laser to deuteron energy when transitioning into the high-fluence regime.

We note that previous work [16] performed on the Titan laser using a 9 ps pulse duration and 360 J of laser energy produced similar results to the 250 J case shown in Table I. In that work, the laser-to-proton conversion efficiency was found to be 0.47% and the laser-to-deuteron efficiency was found to be 0.04%. The maximum proton and deuteron energies were found to be around 17 MeV and around 8 MeV, respectively, in that work. Comparing the 360 J Titan shot with the 1 kJ OMEGA shot, we see a 15× increase in laser-to-deuteron efficiency with only a 2.8× increase in laser energy.

IV. PARTICLE-IN-CELL SIMULATIONS

To better understand our data, we ran simulations using the implicit, hybrid particle-in-cell (PIC) code LSP [60] in 2D cylindrical geometry. The simulations modeled the full 9.0 ps duration of the laser with 250 J and 1 kJ. The minimum spatial cell size of 30 nm in the nonuniform grids was chosen considering skin depth of ~40 nm of the target plasma. Simulations conducted with various cell sizes from 10 nm to 100 nm indicated that deuteron acceleration is not fully resolved with a larger than 40 nm cell. The target was modeled as a 25 μm solid density (1.1 g/cm^3) $C^{4+}D_2^+$ foil. A hydrocarbon contaminant layer of one cell (30 nm) at 10^{22} cm^{-3} was added on the target's rear surface to reproduce the total mass of a 5-nm-thick, 6× critical density ($6n_{\text{crit}} \sim 6 \times 10^{21}$ cm^{-3}) layer as keeping the areal density the same. The contaminant layer thickness was chosen based on previous measurements [27,28]. In our simulations, the contaminant layer is composed of only hydrogen, as this is the lowest mass isotope, to reduce computational cost. The portion of the target that will not see the accelerating TNSA field was modeled with a fluid description [61]; this allows the number of macroparticles per cell (4 particles/cell) to be significantly relaxed comparing to typical PIC simulations. On the rear surface of the target where the TNSA is active, each particle species (P, D, and C^{4+}) is treated kinetically with 900 particles/cell.

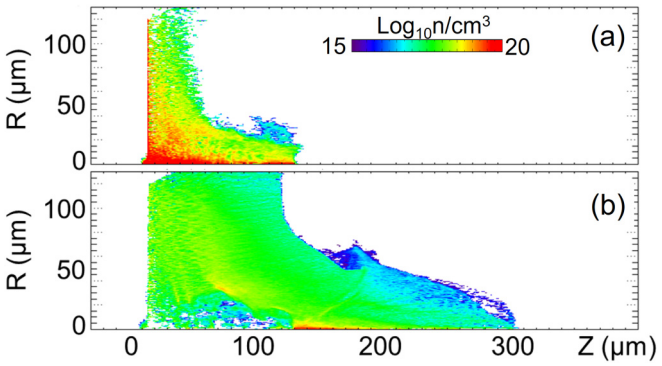

FIG. 3. Pseudocolor images of (a) deuteron and (b) proton densities at a time of 4 ps in the 1 kJ case. In this figure, the electrons are injected from the left side and thus the plasma expansion goes from left to right. The protons have extended further in the z direction due to their higher charge-to-mass ratio. There is a hollow region in the proton density on axis that extends to around $Z = 130$ μm, which corresponds to the region of high deuteron density. Since the deuteron density is highest in this region, it is being accelerated in a unsuppressed manner in this region (i.e., with a higher electric field than in the proton-rich region).

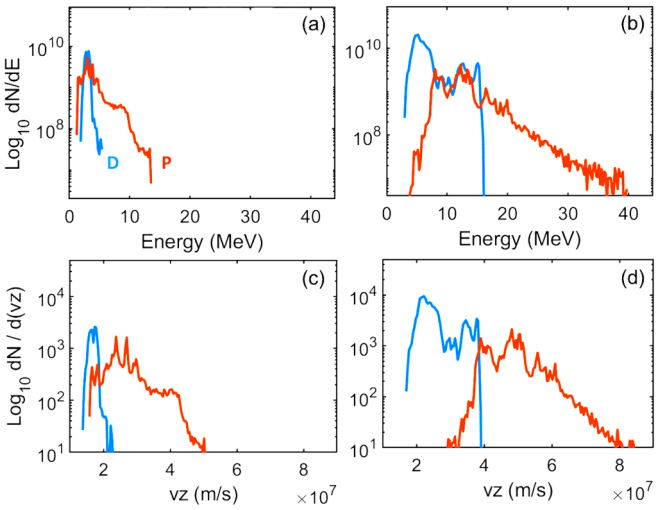

FIG. 4. Simulation measurements of the ion energy (a), (b) and velocity (c), (d) spectra in 250 J case (a), (c) and 1 kJ case (b), (d). P and D represent protons and deuterons. All particles are spatially integrated from the target rear surface to the end of simulation box at 6 ps.

In this multi-ps modeling, electrons were injected to emulate the laser interaction. The electron sources have 9 ps full-width-half-maximum (FWHM) duration with 20 μm FWHM Gaussian spatial profile; this is the same in both the 250 J and 1 kJ simulations and is consistent with the experiment. The energy spectrum had a slope temperature linearly increasing to 4 MeV and 8 MeV until the laser peak for the case of 250 J and 1 kJ lasers. The slope temperatures employed here are based on previously measured experimental data at OMEGA EP, which is similar to Pukhov scaling [62] for the given laser intensity [63]. Utilizing an electron source with increasing slope temperature that exceeds ponderomotive scaling for the laser intensity is a widely used method for simulating particle acceleration from multipicosecond pulses [46,47]. We note that the electron source method used here has been applied previously in similar simulations of ion acceleration [64] and benchmarked against simulations including the electromagnetic interaction of the laser [65]. The authors also checked the electron source method in simulations by comparing the results with simulations done by the explicit full laser simulation and experimental measurements [45,46,66,67].

The modeling results are presented in Fig. 3. Figures 3(a) and 3(b) show the density of the deuteron and proton ions, respectively, at 6 ps for the 1 kJ case. Notice that the protons have expanded much further compared to the heavier (i.e., m_i/Z_i) deuterons. Also, the proton density is hollow toward the target surface. This hollow region corresponds exactly to the region of high deuteron density, and is evidence that here deuterium is dominant in this region.

The simulation results reproduce important features of the experiments. First, we see overall good agreement with many of the energetics, as illustrated in the dN/dE spectra in Figs. 4(a) and 4(b). The maximum deuteron energies, 6 and 20 MeV for 250 J and 1 kJ, respectively, and proton energies agree well with the experiment. Also, we see a 20× increase in the total deuteron yield generated by the 1 kJ case compared to the 250 J case, indicating that deuteron yield is not simply proportional to laser energy. An additional notable feature that is also seen in the experimental data is the similar slope of dN/dE for both deuterons and protons in the 1 kJ case, Fig. 4(d), as opposed to different slopes clearly seen from the 250 J case, Fig. 4(c). This is something that is also observed experimentally.

The simulations also help to illustrate the cause of the dip in proton energies around 8 MeV and the smooth transition in velocity space between protons and deuterons, which are indicators of the transition from suppressed into unsuppressed acceleration. The physics behind this transition can be explained in the following manner: At early times, the edge of the target is proton-rich, which means that the charge-to-mass ratio of the protons sets the strength of the accelerating electric field, $E_{ss} \propto T_e/C_{si} = (T_e m_i/Z_i)^{1/2}$. As the protons have a higher charge-to-mass ratio, they are accelerated more rapidly than the deuterons. Thus, given enough laser energy and time, the proton density is reduced enough that the region near the target becomes deuteron-rich. At this point, the larger mass-to-charge ratio of deuterons creates a stronger electric field leading to more efficient deuteron acceleration. The deuterons cannot overtake the protons in velocity, otherwise they would again become the lower density species and the electric field would decrease. This results in a hollow region in space (see Fig. 3) and a sharp cutoff in velocity space that is seen both experimentally, Fig. 2(d), and in the simulations, Fig. 4(d), in the 1 kJ cases. Additionally, because the field is stronger in the high region with high deuteron density, the protons to be accelerated faster out of this region and into the region with higher proton density; thus creating the dip in energy (velocity) spectra around 8 MeV in Figs. 2(b) and 2(d).

To understand the underlying physics behind the acceleration of deuterons and protons, a series of simulations were conducted to systematically study the different regimes of

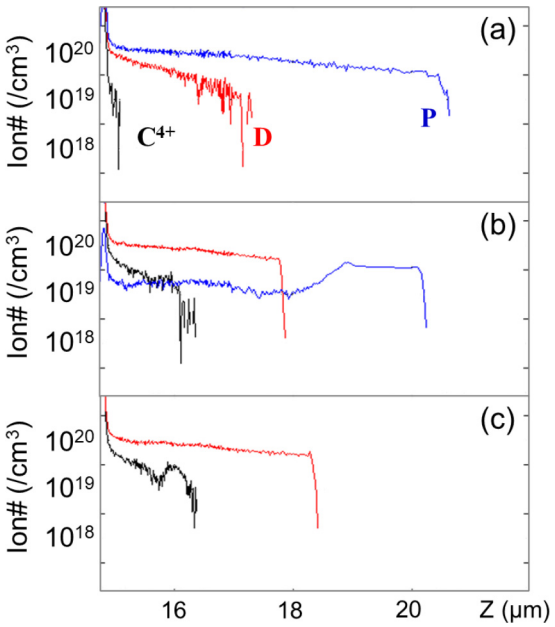

FIG. 5. Density line-outs of proton, deuteron, and carbon ions, in the Z direction measured at 0.5 ps, from a systematic study of the initial hydrogen layer density in the high fluence case. The initial density of hydrogen layer attached to the back surface of CD_2 target is $20n_{crit}$ ($\sim 2 \times 10^{22}$ cm^{-3}) and $6n_{crit}$ ($\sim 6 \times 10^{21}$ cm^{-3}) for (a) and (b), respectively; no hydrogen layer is initialized in (c). The hot electron source, injected continuously up to 1 ps, is identical for all cases

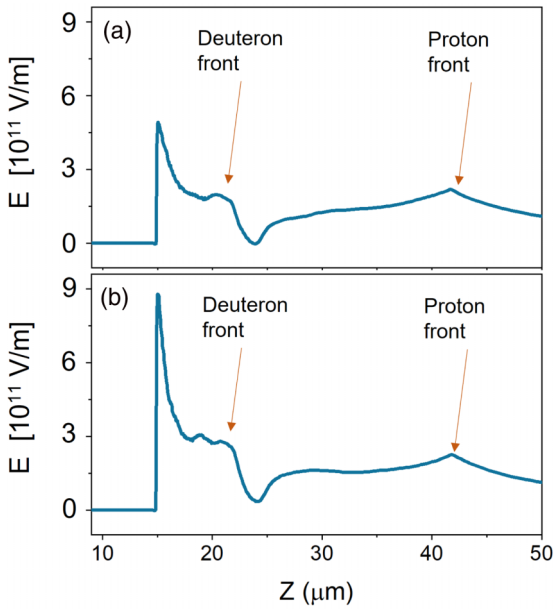

FIG. 6. Profiles of the electric field at 1 ps in the Z direction along the axis for a case of a laser with (a) 0.5 ps and (b) 1 ps duration. In the case with the longer pulse duration, the electric field is significantly higher in the deuteron-rich region nearer to the target. This is due to the increased supply of electrons that drive the electric field.

suppressed and unsuppressed ion acceleration. These were run with electrons injected similarly to the high-fluence case, but with a shorter, 1 ps laser pulse duration to reduce numerical expense. Similar to previous studies [47], deuteron acceleration in simulations appears to highly depend on H contaminant layer initially appended on the rear surface of the target [50]. This is evident from the comparison of ion density in Figs. 5(a)–5(c), where the contaminant layer density is decreased from $20n_{crit}$ to $6n_{crit}$ to zero ($n_{crit} \sim 10^{21}$ cm^{-3}), respectively. In the case where the contaminants are initialized at $20n_{crit}$, Fig. 5(a), the proton density is higher than deuteron density throughout the entire acceleration region. Thus, the entire acceleration region is proton rich, leading to poor deuteron acceleration efficiency. At the other extreme is the case where no protons are included, Fig. 5(c). Here the deuteron density becomes much higher and thus the deuteron acceleration is unsuppressed, leading to much higher acceleration efficiency. Finally, in the intermediate case with a $6n_{crit}$ contaminant layer, Fig. 5(b), there are both proton-rich and deuteron-rich regions. The region closer to the initial target surface, $z < 18$ μm, is deuteron rich and thus the deuterons are accelerated efficiently in this region. The spatial extent of the deuterons is reduced compared to the contaminant-free simulation but still is much improved compared to the $20n_{crit}$ case.

Another important aspect of this paper is the importance of pulse duration on ion acceleration. When the laser starts interacting with a target, protons from the outermost contamination layer on the target surface are exposed to the highest field gradients and screen the electric field for protons and ions coming from the successive layers. This is a heterogeneous condition (e.g., suppressed acceleration) at early time where protons are accelerated first, as they have the highest charge-to-mass ratio. However, if the laser pulse is long, for example, multi-ps used in our paper, the supply of hot electrons continues as the ions are accelerated from the rear surface. Thus, when the protons and deuterons have separated, the electrons traverse the expanding ions and create separate expansion fronts at the edge of the individual ion species. In this condition, the deuterons have a higher density than the protons and thus are unsuppressed in their acceleration. Many hot electrons drive electric field for deuteron acceleration instead of continuing to move further to reach all the way to the proton beam front. Figure 6 shows a comparison of the longitudinal electric field at 1 ps in two simulations where all parameters are identical with the exception of the laser pulse duration: Pulse length of 0.5 ps in Fig. 6(a) and 1 ps in Fig. 6(b). It is clearly seen that with a longer pulse, the electric field at the deuteron front is higher while the electric field near the proton front is similar to the shorter pulse case. This is due to the increased amount of hot electrons near the target surface when using a longer laser pulse duration.

Using the PIC simulations, we also investigated the importance of high laser energy flux on the heating of the target rear surface. During the acceleration, protons initially in the target's rear surface expand in both directions due to target heating. This expansion is influenced by the temperature and pressure of the background electrons. Thus, if the bulk electrons in the target are hotter, it leads to a lower proton density and allows the deuterons to become the dominant species earlier in time. Our simulations found that that proton

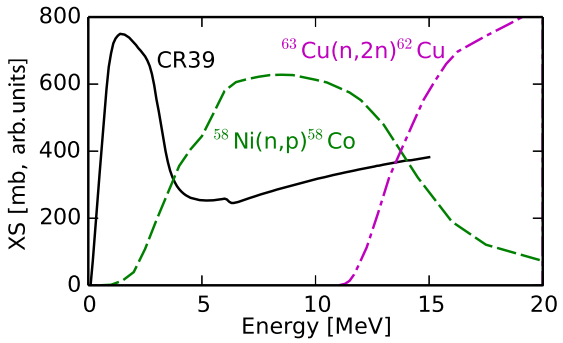

FIG. 7. Lines of normalized CR39 efficiency (solid) and cross sections of ^{58}Ni, $(np)^{58}$Co (dashed) and ^{63}Cu$(n, 2n)^{62}$Cu (dash-dotted).

expansion into the target becomes significant from the case of the high-flux, high-temperature target. A combination of these effects helps understand the 100-fold increase in conversion of laser to deuteron for the high fluence case while only a 4.5-fold increase in conversion of laser to proton compared to low fluence case.

V. NEUTRON GENERATION

To measure the high-energy neutron generation on the experiment, the Proton Film Pack (PFPII) diagnostic was modified to incorporate CR39 plastic and activation foils of (naturally abundant) Ni and Cu at 0° and 90° with respect to the rear surface of the target. Additionally, CR39 foils in the wedge-range-filter diagnostic were placed at 117°. CR39 is a plastic that is indirectly sensitive to neutrons via, predominantly, knock-on reactions with protons in the plastic [68], it is sensitive to a broad range of neutron energies as shown in Fig. 7. We note that CR39 is sensitive to ions and for this reason was placed behind the metal activation foils to shield from accelerated ions. The measured activation product from the Ni foils was ^{58}Co; created via the ^{58}Ni(n,p) reaction. Similar to CR39, the ^{58}Ni(n,p) cross section is sensitive to a broad energy of neutrons (Fig. 7). The long half-life of ^{58}Co (70.9 days) allowed it to be measured of fsite at Lawrence Livermore National Laboratory (LLNL) using high-sensitivity Germanium detectors to measure decay radiation from the 810.8 keV line. We note that on some of the shots, small levels of ^{57}Co were detected, possibly from ^{58}Ni(n,d) or ^{58}Ni(n,np). However, the longer half life of this isotope (272 days) and lower expected activity did not allow for sufficient statistics in the measurement duration. The radioactivity in the Cu foils using an on-site coincidence counter and the decay curves were fit with two exponential decays corresponding to the half lives of ^{62}Cu (9.6 minutes) and ^{64}Cu (12.7 hours). We note the possibility of activation of ^{63}Zn (38.5 min) via ^{63}Cu(p,n) reactions, but foils were shielded to avoid proton irradiation. The isotope used in this measurement was ^{62}Cu from ^{63}Cu$(n, 2n)$ which, unlike the other yield measurements, is only sensitive to high-energy neutrons above around 11 MeV (see Fig. 7). A difficulty in using an $(n,2n)$ reaction is that the same products are created from a (γ, n) reaction, which could potentially corrupt the measurement. To account for this, we used a null shot (Cu foil only, no LiF) which gave a low yield compared to the highest measured neutron yield (∼10%) that was subtracted from the data and used as an error bar. The null shot was taken when measuring the ion acceleration, meaning that the RCF obstructed the 0° view and thus we were not able to attain a null value at 0°. Therefore, we did not use the 0° data for Cu, which we expect to be highly compromised by x-ray radiation that is known to peak on axis. As for ^{64}Cu, the cross section of ^{65}Cu$(n,2n)$ is high enough to be useful. However, the existence of ^{63}Cu(n, γ) capturing a reaction with high sensitivity to low energy meant that this measurement was affected by thermal neutrons and was therefore not used.

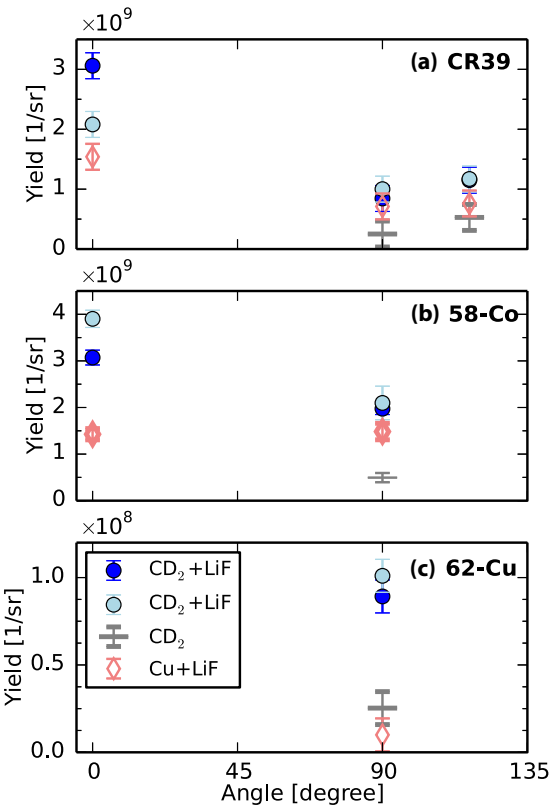

FIG. 8. (a)–(c) Neutron yields inferred from the CR39 and activation foils for different setups: $CD_2 + LiF$ (circles), CD_2 alone (bars), and $Cu + LiF$ (diamonds). The CR39 was analyzed using an estimated neutron spectrum to create an average efficiency from which to infer the yield. The ^{58}Co and ^{62}Cu data used average cross sections of 400 and 350 mb, respectively. Error bars are taken as the value of null shots irradiating a Cu foil alone.

Figure 8 shows the yields recorded from CR39 and activation foils; the shots using $CD_2 + LiF$ converter were compared against shots with a CD_2 target alone and $Cu + LiF$. All shots are with 1 kJ of laser energy. We make a number of observations from this data. First, we see that the broadband yield (i.e., CR39 and ^{58}Co) at angles larger than 90° are 20% to 50% higher in $CD_2 + LiF$ compared to $Cu + LiF$. We attribute this to the fact that the protons accelerated by both Cu and CD_2 are similar, and that the deuterons contribute only modestly to broadband neutron generation. Second, we see an increase of around a factor of 2× in broadband neutron generation in the forward direction in the $CD_2 + LiF$

compared to Cu + LiF. This is expected from the fact that there is a break-up reaction in deuterium, which is known to be highly forward biased. Such results have been seen previously in a high-intensity laser context [17,19]. Finally, we observe a dramatic, 10× increase in high-energy neutrons from the ^{62}Cu data in CD_2 + LiF compared to Cu + LiF. This is due to the high, 15 MeV, Q value of the ^{7}Li(d,n) reaction, compared to 3.3 MeV for ^{2}D(d,n) reactions and −1.6 MeV (i.e., endothermic) for ^{7}Li(p,n).

Note that in all neutron measurements, the CD_2 case is substantially lower than the CD_2 + LiF. This indicates that the majority of the neutron generation comes from protons and deuterons accelerated from the rear surface of the foil and not from the CD_2 target itself. Generally, the yield from Cu + LiF is larger than CD_2 alone. The exceptions to this are high-energy neutrons (^{62}Cu data), which are expected due to the fact that D(d,n) reactions, like ^{7}Li(d,n), are exothermic.

A finding that was at first surprising was the increase in yield as compared to previous work on the Titan laser [16]. On OMEGA EP, we see only 4× increase in yield compared to Titan, where a 360 J laser was used (2.8× lower energy), also with a 9 ps pulse length. Given the 100× increase in deuteron acceleration efficiency observed in this work, an increase of only 4× seems too small. To better understand this, we performed analytical calculations of the expected neutron yields using the measured proton and deuteron spectra. The calculations propagated ions through a 2 mm LiF block. Ions lost energy via collisional stopping using stopping powers calculated from the code SRIM [69]. Total neutron yields were generated using the appropriate cross sections for ^{7}Li(d,n) [70], ^{7}Li(p,n) [71], and ^{19}F (p, n) [72,73] as the ions traversed the LiF. For the 1 kJ shot, this calculation gave an estimate of 9.2×10^8 and 6.3×10^8 neutrons/sr angularly averaged neutron fluence generated by the protons and deuterons, respectively. The total number of neutrons, 1.6×10^9 sr^{-1}, agrees well with the broadband neutron production (i.e., CR39 at >90°, ^{58}Co at 90°) shown in Fig. 8. This calculation shows that around 60% for the neutrons are due to protons and 40% are due to deuterons. This is consistent with the reduction in broadband neutron yield from CD_2 + LiF compared with Cu + LiF, given that we expect similar proton spectra in the two cases and given that Cu will not accelerate deuterons. When using the measured ion spectra in the 250 J case, the importance of deuterons is found to be dramatically reduced; deuterons account for only 2% of the total neutrons production. Given that deuterons play a negligible role in the total neutron yield a lower laser energies, a factor of 4× increase in yield from our work the 360 J shot on Titan is reasonable, especially considering that we see an increase in proton acceleration efficiency of 4.5× in this experiment.

The neutron yields from this paper are comparable to the Trident laser yields utilizing the BOA mechanism [17], which used a laser intensity around an order of magnitude higher. Herein, we have quantified the number of highest energy neutrons (>11 MeV), which are around 3% of the total yield.

VI. SUMMARY

In summary, we have performed laser ion acceleration experiments in the high-fluence (>1 J/μm^2) hydrocarbon contaminant layer depletion regime. This led to a 100× increase of laser energy coupled into deuterons from the bulk of the target (0.6 ± 0.1%) as well as increased maximum deuteron energy as compared to the protons. However, the coupling of laser energy is still predominantly into protons (4.5%). This leaves a wide space that can be explored when much higher energy lasers come online, such as ARC [40–42] (14 kJ) at the LLNL and PETAL [43,44] (6 kJ) at Laser Megajoule in France. If these attain laser spot diameters equal to or smaller than OMEGA EP, fluence of above 10× is attainable. This will lead to self-cleaning of the targets of contaminants and a marked increase in bulk-ion acceleration that will likely exceed the protons in both efficiency and maximum kinetic energy. Increased fluence will thus allow researchers to choose a variety of different ions for acceleration. This can lead to improvements in a number of applications, for example, better performance in terms of isochoric heating by allowing the stopping power to be varied, in terms of electromagnetic field measurements by allowing the charge-to-mass ratio to be varied, in terms of high-energy short-pulse neutron generation by increasing the number of deuterons and allowing reactions with other ion species to be explored, and for any use of laser-accelerated ions that are presently constrained to the mass, the charge, and the charge-to-mass ratio of protons.

ACKNOWLEDGMENTS

This work was performed under the auspices of the U.S. Department of Energy by Lawrence Livermore National Laboratory under Contract No. DE-AC52-07NA27344. G.P. was supported by the NRL Base Program.

[1] A. P. Fews, P. A. Norreys, F. N. Beg, A. R. Bell, A. E. Dangor, C. N. Danson, P. Lee, and S. J. Rose, Plasma Ion Emission from High Intensity Picosecond Laser Pulse Interactions with Solid Targets, Phys. Rev. Lett. **73**, 1801 (1994).

[2] E. L. Clark, K. Krushelnick, J. R. Davies, M. Zepf, M. Tatarakis, F. N. Beg, A. Machacek, P. A. Norreys, M. I. K. Santala, and I. Watts, Measurements of Energetic Proton Transport through Magnetized Plasma from Intense Laser Interactions with Solids, Phys. Rev. Lett. **84**, 670 (2000).

[3] R. A. Snavely, M. H. Key, S. P. Hatchett, T. E. Cowan, M. Roth, T. W. Phillips, M. A. Stoyer, E. A. Henry, T. C. Sangster, and M. S. Singh, Intense High-Energy Proton Beams from Petawatt-Laser Irradiation of Solids, Phys. Rev. Lett. **85**, 2945 (2000).

[4] J. Fuchs, P. Antici, E. D'Humières, E. Lefebvre, M. Borghesi, E. Brambrink, C. A. Cecchetti, M. Kaluza, V. Malka, M. Manclossi, S. Meyroneinc, P. Mora, J. Schreiber, T. Toncian, H. Pépin, and P. Audebert, Laser-driven proton scaling laws and new paths towards energy increase, Nat. Phys. **2**, 48 (2006).

[5] L. Robson, P. T. Simpson, R. J. Clarke, K W D Ledingham, F. Lindau, O. Lundh, T. Mccanny, P. Mora, D. Neely, C. G. Wahlström, M. Zepf, and P. Mckenna, Scaling of proton acceleration driven by petawatt-laser–plasma interactions, Nat. Phys. **3**, 58 (2007).

[6] S. N. Chen, E. d'Humiéres, E. Lefebvre, L. Romagnani, T. Toncian, P. Antici, P. Audebert, E. Brambrink, C. A. Cecchetti, T. Kudyakov *et al.*, Focusing Dynamics of High-Energy Density, Laser-Driven Ion Beams, Phys. Rev. Lett. **108**, 055001 (2012).

[7] L. Lancia, B. Albertazzi, C. Boniface, A. Grisollet, R. Riquier, F. Chaland, K.-C. Le Thanh, Ph. Mellor, P. Antici, S. Buffechoux *et al.*, Topology of Megagauss Magnetic Fields and of Heat-Carrying Electrons Produced in a High-Power Laser-Solid Interaction, Phys. Rev. Lett. **113**, 235001 (2014).

[8] L. Gao, P. M. Nilson, I. V. Igumenshchev, M. G. Haines, D. H. Froula, R. Betti, and D. D. Meyerhofer, Precision Mapping of Laser-Driven Magnetic Fields and Their Evolution in High-Energy-Density Plasmas, Phys. Rev. Lett. **114**, 215003 (2015).

[9] C. Goyon, B. B. Pollock, D. P. Turnbull, A. Hazi, L. Divol, W. A. Farmer, D. Haberberger, J. Javedani, A. J. Johnson, A. Kemp *et al.*, Ultrafast probing of magnetic field growth inside a laser-driven solenoid, Phys. Rev. E **95**, 033208 (2017).

[10] M. Roth, T. E. Cowan, M. H. Key, S. P. Hatchett, C. Brown, W. Fountain, J. Johnson, D. M. Pennington, R. A. Snavely, S. C. Wilks *et al.*, Fast Ignition by Intense Laser-Accelerated Proton Beams, Phys. Rev. Lett. **86**, 436 (2001).

[11] Dustin Theodore Offermann, K. A. Flippo, J. Cobble, M. J. Schmitt, S. A. Gaillard, T. Bartal, D. V. Rose, D. R. Welch, M. Geissel, and M. Schollmeier, Characterization and focusing of light ion beams generated by ultra-intensely irradiated thin foils at the kilojoule scale, Phys. Plasmas **18**, 056713 (2011).

[12] T. Bartal, M. E. Foord, C. Bellei, M. H. Key, K. A. Flippo, S. A. Gaillard, D. T. Offermann, P. K. Patel, L. C. Jarrott, D. P. Higginson *et al.*, Focusing of short-pulse high-intensity laser-accelerated proton beams, Nat. Phys. **8**, 139 (2012).

[13] P. K. Patel, A. J. Mackinnon, M. H. Key, T. E. Cowan, M. E. Foord, M. Allen, D. F. Price, H. Ruhl, P. T. Springer, and R. Stephens, Isochoric Heating of Solid-Density Matter with an Ultrafast Proton Beam, Phys. Rev. Lett. **91**, 125004 (2003).

[14] K. L. Lancaster, S. Karsch, H. Habara, F. N. Beg, E. L. Clark, R. Freeman, M. H. Key, J. A. King, R. Kodama, K. Krushelnick, K. W. D. Ledingham, P. McKenna, C. D. Murphy, P. A. Norreys, R. Stephens, C. Stoeckl, Y. Toyama, M. S. Wei, and M. Zepf, Characterization of Li(p, n)Be neutron yields from laser produced ion beams for fast neutron radiography, Phys. Plasmas **11**, 3404 (2004).

[15] D. P. Higginson, J. M. McNaney, D. C. Swift, T. Bartal, D. S. Hey, R. Kodama, S. Le Pape, A. Mackinnon, D. Mariscal, H. Nakamura, N. Nakanii, K. A. Tanaka, and F. N. Beg, Laser generated neutron source for neutron resonance spectroscopy, Phys. Plasmas **17**, 100701 (2010).

[16] D. P. Higginson, J. M. McNaney, D. C. Swift, G. M. Petrov, J. Davis, J. A. Frenje, L. C. Jarrott, R. Kodama, K. L. Lancaster, A. J. Mackinnon *et al.*, Production of neutrons up to 18 MeV in high-intensity, short-pulse laser matter interactions, Phys. Plasmas **18**, 100703 (2011).

[17] M. Roth, D. Jung, K. Falk, N. Guler, O. Deppert, M. Devlin, A. Favalli, J. Fernandez, D. Gautier, M. Geissel *et al.*, Bright Laser-Driven Neutron Source Based on the Relativistic Transparency of Solids, Phys. Rev. Lett. **110**, 044802 (2013).

[18] D. P. Higginson, L. Vassura, M. M. Gugiu, P. Antici, M. Borghesi, S. Brauckmann, C. Diouf, A. Green, L. Palumbo, H. Petrascu *et al.*, Temporal Narrowing of Neutrons Produced by High-Intensity Short-Pulse Lasers, Phys. Rev. Lett. **115**, 054802 (2015).

[19] S. Kar, A. Green, H. Ahmed, A. Alejo, A. P. L. Robinson, M. Cerchez, R. Clarke, D. Doria, S. Dorkings, J. Fernandez *et al.*, Beamed neutron emission driven by laser accelerated light ions, New J. Phys. **18**, 053002 (2016).

[20] R. T. Khaydarov, H. B. Beisinbaeva, M. M. Sabitov, V. B. Terentev, and G. R. Berdiyorov, Effect of neutron irradiation on the characteristics of laser-produced plasma, Nucl. Fusion **50**, 025024 (2010).

[21] L. J. Perkins, B. G. Logan, M. D. Rosen, M. D. Perry, T. D. de La Rubia, N. M. Ghoniem, T. Ditmire, P. T. Springer, and S. C. Wilks, The investigation of high intensity laser driven micro neutron sources for fusion materials research at high fluence, Nucl. Fusion **40**, 1 (2000).

[22] J. D. Sethian, A. R. Raffray, J. Latkowski, J. P. Blanchard, L. Snead, T. J. Renk, and S. Sharafat, An overview of the development of the first wall and other principal components of a laser fusion power plant, J. Nucl. Mater. **347**, 161 (2005).

[23] U. Fischer, M. Avrigeanu, P. Pereslavtsev, S. P. Simakov, and I. Schmuck, Evaluation and validation of d-Li cross section data for the IFMIF neutron source term simulation, J. Nucl. Mater. **367-370**, 1531 (2007).

[24] V. W Yuan, J. D. Bowman, D. J. Funk, G. L. Morgan, R. L. Rabie, C. E. Ragan, J. P. Quintana, and H. L. Stacy, Shock Temperature Measurement using Neutron Resonance Spectroscopy, Phys. Rev. Lett. **94**, 125504 (2005); D. C. Swift, A. Seifter, D. Holtkamp, V. Yuan, D. Bowman, and D. A. Clark, Explanation of anomalous shock temperatures in shock-loaded Mo samples measured using neutron resonance spectroscopy, Phys. Rev. B **77**, 092102 (2008).

[25] S. C. Wilks, A. B. Langdon, T. E. Cowan, M. Roth, M. Singh, S. Hatchett, M. H. Key, D. Pennington, A. MacKinnon, and R. A. Snavely, Energetic proton generation in ultra-intense laser–solid interactions, Phys. Plasmas **8**, 542 (2001).

[26] S. C. Wilks, W. L. Kruer, M. Tabak, and A. B. Langdon, Absorption of Ultra-Intense Laser Pulses, Phys. Rev. Lett. **69**, 1383 (1992).

[27] M. Allen, P. K. Patel, A. Mackinnon, D. Price, S. Wilks, and E. Morse, Direct Experimental Evidence of Back-Surface Ion Acceleration from Laser-Irradiated Gold Foils, Phys. Rev. Lett. **93**, 265004 (2004).

[28] M. M. Allen, Ion acceleration from the interaction of ultra-intense lasers with solid foils, Ph.D. thesis, University of California, Berkeley, 2004

[29] M. Hegelich, S. Karsch, G. Pretzler, D. Habs, K. Witte, W. Guenther, M. Allen, A. Blazevic, J. Fuchs, J. C. Gauthier, M. Geissel, P. Audebert, T. Cowan, and M. Roth, MeV Ion Jets from Short-Pulse-Laser Interaction with Thin Foils, Phys. Rev. Lett. **89**, 085002 (2002).

[30] J. T. Morrison, M. Storm, E. Chowdhury, K. U. Akli, S. Feldman, C. Willis, R. L. Daskalova, T. Growden, P. Berger, T. Ditmire *et al.*, Selective deuteron production using target normal sheath acceleration, Phys. Plasmas **19**, 030707 (2012).

[31] A. G. Krygier, J. T. Morrison, S. Kar, H. Ahmed, A. Alejo, R. Clarke, J. Fuchs, A. Green, D. Jung, A. Kleinschmidt *et al.*, Selective deuterium ion acceleration using the Vulcan petawatt laser, Phys. Plasmas **22**, 053102 (2015).

[32] A. Maksimchuk, A. Raymond, F. Yu, G. M. Petrov, F. Dollar, L. Willingale, C. Zulick, J. Davis, and K. Krushelnick, Dominant deuteron acceleration with a high-intensity laser for isotope production and neutron generation, Appl. Phys. Lett. **102**, 191117 (2013).

[33] A. Alejo, A. G. Krygier, H. Ahmed, J. T. Morrison, R. J. Clarke, J. Fuchs, A. Green, J. S. Green, D. Jung, A. Kleinschmidt *et al.*, High flux, beamed neutron sources employing deuteron-rich ion beams from D_2 O-ice layered targets, Plasma Phys. Controlled Fusion **59**, 064004 (2017).

[34] P. A. Norreys, A. P. Fews, F. N. Beg, A. R. Bell, A. E. Dangor, P. Lee, M. B. Nelson, H. Schmidt, M. Tatarakis, and M. D. Cable, Neutron production from picosecond laser irradiation of deuterated targets at intensities of 10^{19} W cm^{-2}, Plasma Phys. Controlled Fusion **40**, 175 (1998).

[35] L. Disdier, J. P. Garconnet, G. Malka, and J. L. Miquel, Fast Neutron Emission from a High-Energy Ion Beam Produced by a High-Intensity Subpicosecond Laser Pulse, Phys. Rev. Lett. **82**, 1454 (1999).

[36] L. Willingale, G. M. Petrov, A. Maksimchuk, J. Davis, R. R. Freeman, A. S. Joglekar, T. Matsuoka, C. D. Murphy, V. M. Ovchinnikov, A. G. R. Thomas *et al.*, Comparison of bulk and pitcher-catcher targets for laser-driven neutron production, Phys. Plasmas **18**, 083106 (2011).

[37] L. Yin, B. J. Albright, B. M. Hegelich, and J. C. Fernández, GeV laser ion acceleration from ultrathin targets: The laser break-out afterburner, Laser Part. Beams **24**, 291 (2006).

[38] L. Yin, B. J. Albright, B. M. Hegelich, K. J Bowers, K. A. Flippo, T. J. T. Kwan, and J. C. Fernández, Monoenergetic and GeV ion acceleration from the laser breakout afterburner using ultrathin targets, Phys. Plasmas **14**, 056706 (2007).

[39] D. Jung, K. Falk, N. Guler, O. Deppert, M. Devlin, A. Favalli, J. C. Fernandez, D. C. Gautier, M. Geissel, R. Haight *et al.*, Characterization of a novel, short pulse laser-driven neutron source, Phys. Plasmas **20**, 056706 (2013).

[40] J. K. Crane, G. Tietbohl, P. Arnold, E. S. Bliss, C. Boley, G. Britten, G. Brunton, W. Clark, J. W. Dawson, S. Fochs *et al.*, Progress on converting a NIF quad to eight, petawatt beams for advanced radiography, J. Phys.: Conf. Ser. **244**, 032003 (2010).

[41] J. M. Di Nicola, S. T. Yang, C. D. Boley, J. K. Crane, J. E. Heebner, T. M. Spinka, P. Arnold, C. P. J. Barty, M. W. Bowers, T. S. Budge *et al.*, The commissioning of the advanced radiographic capability laser system: Experimental and modeling results at the main laser output, Proc. SPIE **9345**, 93450I (2015).

[42] H. Chen, M. R. Hermann, D. H. Kalantar, D. A. Martinez, P. Di Nicola, R. Tommasini, O. L. Landen, D. Alessi, M. Bowers, D. Browning *et al.*, High-energy (>70 kev) x-ray conversion efficiency measurement on the ARC laser at the National Ignition Facility, Phys. Plasmas **24**, 033112 (2017).

[43] N. Blanchot, G. Behar, T. Berthier, E. Bignon, F. Boubault, C. Chappuis, H. Coïc, C. Damiens-Dupont, J. Ebrardt, Y. Gautheron *et al.*, Overview of PETAL, the multi-petawatt project on the LIL facility, Plasma Phys. Controlled Fusion **50**, 124045 (2008).

[44] J. L. Miquel, C. Lion, and P. Vivini, The laser mega-joule: LMJ & PETAL status and program overview, J. Phys.: Conf. Ser. **688**, 012067 (2016).

[45] A. Yogo, K. Mima, N. Iwata, S. Tosaki, A. Morace, Y. Arikawa, S. Fujioka, T. Johzaki, Y. Sentoku, H. Nishimura *et al.*, Boosting laser-ion acceleration with multi-picosecond pulses, Sci. Rep. **7**, 42451 (2017).

[46] J. Kim, A. J. Kemp, S. C. Wilks, D. H. Kalantar, S. Kerr, D. Mariscal, F. N. Beg, C. McGuffey, and T. Ma, Computational modeling of proton acceleration with multi-picosecond and high energy, kilojoule, lasers, Phys. Plasmas **25**, 083109 (2018).

[47] D. Mariscal, T. Ma, S. C. Wilks, A. J. Kemp, G. J. Williams, P. Michel, H. Chen, P. K. Patel, B. A. Remington, M. Bowers *et al.*, First demonstration of ARC-accelerated proton beams at the National Ignition Facility, Phys. Plasmas **26**, 043110 (2019).

[48] R. P. Drake, *High-Energy-Density Physics* (Springer, Berlin, 2006), Chaps. 8, 10, pp. 335–365, 423–448.

[49] Previous work at the Prague Asterix Laser System has focused on longer pulses (0.6 kJ, 300 ps) to accelerate front-surface ions [74,75], but did not focus on the rear-surface ions of interest in this paper. Also, previous work on the OMEGA EP laser (1 kJ, 10 ps) accelerated carbon ions from the bulk target by cleaning the target via laser-heating [11], but did not look at the depletion of the contaminant layer without laser-heating.

[50] G. M. Petrov, L. Willingale, J. Davis, Tz Petrova, A. Maksimchuk, and K. Krushelnick, The impact of contaminants on laser-driven light ion acceleration, Phys. Plasmas **17**, 103111 (2010).

[51] A. V. Gurevich, L. V. Pariiskaya, and L. P. Pitaevskii, Zh. Eksp. Teor. Fiz. **49**, 647 (1965) [Sov. Phys. JETP 22, 449 (1966)].

[52] J. E. Crow, P. L. Auer, and J. E. Allen, Expansion of a plasma into a vacuum, J. Plasma Phys. **14**, 65 (1975).

[53] P. Mora, Plasma Expansion into a Vacuum, Phys. Rev. Lett. **90**, 185002 (2003).

[54] L. M. Wickens and J. E. Allen, Ion emission from laser-produced, multi-ion species, two-electron temperature plasmas, Phys. Fluids **24**, 1894 (1981).

[55] V. T. Tikhonchuk, A. A. Andreev, S. G. Bochkarev, and V. Yu. Bychenkov, Ion acceleration in short-laser-pulse interaction with solid foils, Plasma Phys. Controlled Fusion **47**, B869 (2005).

[56] C. Dorrer, A. Consentino, D. Irwin, J. Qiao, and J. D. Zuegel, OPCPA front end and contrast optimization for the OMEGA EP kilojoule, picosecond laser, J. Opt. **17**, 094007 (2015).

[57] J. A. Cobble, K. A. Flippo, D. T. Offermann, F. E. Lopez, J. A. Oertel, D. Mastrosimone, S. A. Letzring, and N. Sinenian, High-resolution Thomson parabola for ion analysis, Rev. Sci. Instrum. **82**, 113504 (2011).

[58] V. Lelasseux and J. Fuchs, Modelling energy deposition in TR image plate detectors for various ion types, J. Instrum. **15**, P04002 (2020).

[59] D. S. Hey, M. H. Key, A. J. Mackinnon, A. G. MacPhee, P. K. Patel, R. R. Freeman, L. D. Van Woerkom, and C. M. Castaneda, Use of GafChromic film to diagnose laser generated proton beams, Rev. Sci. Instrum. **79**, 053501 (2008).

[60] D. R. Welch, D. V. Rose, M. E. Cuneo, R. B. Campbell, and T. A. Mehlhorn, Integrated simulation of the generation and transport of proton beams from laser-target interaction, Phys. Plasmas **13**, 063105 (2006).

[61] C. Thoma, D. R. Welch, R. E. Clark, N. Bruner, J. J. MacFarlane, and I. E. Golovkin, Two-fluid electromagnetic simulations of plasma-jet acceleration with detailed equation-of-state, Phys. Plasmas **18**, 103507 (2011).

[62] A. Pukhov, Z.-M. Sheng, and J. Meyer-ter Vehn, Particle acceleration in relativistic laser channels, Phys. Plasmas **6**, 2847 (1999).

[63] H. Chen, A. Link, Y. Sentoku, P. Audebert, F. Fiuza, A. Hazi, R. F. Heeter, M. Hill, L. Hobbs, A. J. Kemp *et al.*, The scaling of electron and positron generation in intense laser-solid interactions, Phys. Plasmas **22**, 056705 (2015).

[64] M. E. Foord, T. Bartal, C. Bellei, M. Key, K. Flippo, R. B. Stephens, P. K. Patel, H. S. McLean, L. C. Jarrott, M. S. Wei *et al.*, Proton trajectories and electric fields in a laser-accelerated focused proton beam, Phys. Plasmas **19**, 056702 (2012).

[65] B. Qiao, M. E. Foord, M. S. Wei, R. B. Stephens, M. H. Key, H. McLean, P. K. Patel, and F. N. Beg, Dynamics of high-energy proton beam acceleration and focusing from hemisphere-cone targets by high-intensity lasers, Phys. Rev. E **87**, 013108 (2013).

[66] D. P. Higginson, A. Link, H. Sawada, S. C. Wilks, T. Bartal, S. Chawla, C. D. Chen, K. A. Flippo, L. C. Jarrott, M. H. Key *et al.*, High-contrast laser acceleration of relativistic electrons in solid cone-wire targets, Phys. Rev. E **92**, 063112 (2015).

[67] N. Iwata, K. Mima, Y. Sentoku, A. Yogo, H. Nagatomo, H. Nishimura, and H. Azechi, Fast ion acceleration in a foil plasma heated by a multi-picosecond high intensity laser, Phys. Plasmas **24**, 073111 (2017).

[68] J. A. Frenje, C. K. Li, F. H. Séguin, D. G. Hicks, S. Kurebayashi, and R. D. Petrasso, Absolute measurements of neutron yields from DD and DT implosions at the OMEGA laser facility using CR-39 track detectors, Rev. Sci. Instrum. **73**, 2597 (2002).

[69] J. F. Ziegler, *SRIM, the stopping and range of ions in matter* (SRIM Co., Chester, Maryland, 2008).

[70] P. Pereslavtsev, U. Fischer, S. Simakov, and M. Avrigeanu, Evaluation of d + ^{6,7}Li data for deuteron incident energies up to 50 MeV, Nucl. Instrum. Methods Phys. Res., Sect. B **266**, 3501 (2008).

[71] S. N. Abramovich, B. Ja Guzhovskij, V. A. Zherebcov, and A. G. Zvenigorodskij, Estimated values of total and differential cross sections of proton interactions with nuclei Li-6 and Li-7, Vopr. At. Nauki Tekh., Ser.: Yad. Konstanty **114**, 17 (1984).

[72] F. L. Riffle, J. D. Goss, D. R. Parsignault, and J. C. Harris, Measurement of the absolute total cross section for the reaction ^{19}F (p, n)^{19}Ne, Nucl. Phys. A **115**, 120 (1968).

[73] S. wa Kitwanga, P. Leleux, P. Lipnik, and J. Vanhorenbeeck, Production of ^{14,15}O, ^{18}F, and ^{19}Ne radioactive nuclei from (p,n) reactions up to 30 MeV, Phys. Rev. C **42**, 748 (1990).

[74] J. Krása, D. Klír, A. Velyhan, E. Krouský, M. Pfeifer, K. Řezáč, J. Cikhardt, K. Turek, J. Ullschmied, and K. Jungwirth, Generation of high-energy neutrons with the 300-ps-laser system PALS, High Power Laser Sci. Eng. **2**, e19 (2014).

[75] D. Klir, J. Krasa, J. Cikhardt, R. Dudzak, E. Krousky, M. Pfeifer, K. Rezac, O. Sila, J. Skala, J. Ullschmied *et al.*, Efficient neutron production from sub-nanosecond laser pulse accelerating deuterons on target front side, Phys. Plasmas **22**, 093117 (2015).